Experimental determination of the relationship between the elements of a back-to-back diode model for organic photovoltaic cells' S-shaped I-V characteristics and cell structure

View Online   Export Citation   CrossMark

Elisa Sesa,[1] ID Darmawati Darwis,[1] Xiaojing Zhou,[2] Warwick J. Belcher,[2] and Paul C. Dastoor[2,a] ID

AFFILIATIONS

[1] Physics Department, University of Tadulako, Palu, Indonesia

[2] Centre for Organic Electronics, University of Newcastle, Callaghan, NSW 2308, Australia

[a] Corresponding author: Paul.Dastoor@newcastle.edu.au

ABSTRACT

Equivalent circuit models are becoming increasingly important for the development of large scale demonstrations of organic photovoltaics. The 'S' shaped profile is a common feature of OPV current-voltage (I-V) curves and consequently equivalent circuit models that replicate these features are urgently required. In this paper we prepare a case study based on ITO/PEDOT-PSS/P3HT:PCBM/Al devices whose I-V profiles transition from 'S' shape to 'J' shape with increasing aluminium thickness prepared using low evaporation rates. We show that the new back-to-back diode model (B2BDM) not only faithfully models these I-V profiles but, more importantly, that the specific circuit elements in the model directly correlate with the physical structures in OPV devices that determine the 'S' shaped character. On the basis of these observations, the physical interpretation of the B2BDM is discussed.

INTRODUCTION

As organic photovoltaics (OPVs) approach commercial scale production, the need for accurate equivalent circuit modelling of these systems has become more pressing. In particular, electrical models of large scale modular arrays of organic solar cells are required for system optimisation, driven in part by the intrinsic variability of organic photovoltaics.[1] The electrical characteristics of organic photovoltaics (OPVs) are more complex than conventional photovoltaic devices; varying from an ideal 'J' shape to a non-ideal 'S' shape with a 'kink' in the current-voltage (I-V) plot when under AM1.5G illumination.[2]

The origin of the kink in the I-V characteristic under illumination has intrigued researchers over the years with many reports invoking a range of mechanisms to explain the generation of these 'S' shaped electrical characteristics.[3] For example, de Castro et al. reported that isolated metal nanoclusters formed upon cathode evaporation lead to interfacial defect states and change the electric field of the device; resulting in 'S' shaped I-V curves.[4] Wagenpfahl et al. showed that it was possible to experimentally create a kink in the I-V characteristic by extending the oxygen plasma etch on ITO substrates used as the transparent electrode in OPV devices.[5] Kumar et al. obtained the I-V kink by changing the device structure to include a different interfacial layer,[6] while Wang et al. demonstrated that the I-V curves in bilayer heterojunction devices could be systematically changed from 'J' shaped to 'S' shaped by gradually increasing the thickness of an interfacial exciton blocking layer.[7] Zuo et al. showed that 'S'-shaped curves could be produced in planar bilayer devices by creating a rectifying Schottky junction at the anode interface.[8]

Tada showed that the 'S'-shaped characteristic was created in unannealed OPV devices,[9] while Finck argued that S'-shaped curves are caused by factors that affect the extraction of charge at the device cathode.[10]

One of the most common approaches to understanding the electrical characteristics of PV devices is to use an equivalent circuit model to fit the shape of the I-V curve.[11] While the ideal 'J' shaped I-V profile is relatively straightforward to fit using this approach,[12] modelling the more complex 'S' shaped I-V curve has proven to be more challenging with existing models, such as the one diode model (ODM)[13] and two diode model (TDM)[4,12] unable to fit the experimental data across the entire voltage range.

Work in this laboratory has led to the development of a new equivalent circuit model for OPV devices exhibiting 'S' shaped I-V characteristics[14] that has been subsequently applied to explain the I-V behaviour in inorganic $MoS_2:WSe_2$ solar cells[15] and printed P3HT:PCBM OPV devices.[16] This back-to-back diode model (B2BDM) is built up systematically from a minimum number of circuit elements (eight) and is capable of accurately fitting the kink in 'S' shaped I-V curves as well as the I-V characteristic across the entire voltage range.[17] In particular, it is the addition of two back-to-back diodes (corresponding to two semiconducting interfacial junctions, D_1 and D_2) in combination with an interface voltage source, (generating a new internal dipole field, V_{offset}) that provides the voltage dependent inflexion in the I-V curve needed to reproduce the 'S' shaped behaviour. Indeed, this approach has been supported by recent work recognising the importance of a back-to-back diode element[18,19] and associated shunt resistance[20] in accurately modelling 'S' shaped I-V curves. However, none of these more recent equivalent circuit models include the presence of a voltage source; representing the effect of accumulated charges at the interface.

In this paper we systematically change the I-V profile in OPV devices from 'S' to 'J' shaped by varying the top aluminium layer thickness and thus changing the degree of oxidation of the metal cathode. X-ray photoelectron spectroscopy (XPS) depth profiling is used to probe the bulk and interfacial chemical composition of the device architecture; confirming the oxide thickness change. We show that the well-characterised P3HT:PCBM system provides an ideal case study for validating the B2BDM model; demonstrating definitively that the equivalent circuit elements in the B2BDM are directly correlated with real physicochemical structures within the OPV device. Consequently, we highlight that the B2BDM provides a quantitatively meaningful representation of the device's electronic structure.

EXPERIMENTAL

Device fabrication

Patterned indium tin oxide (ITO) substrates were sourced from Kintec with a sheet resistance of 15 Ω/∞ and an optical transmission of greater than 80%. The pre-patterned ITO slides were cleaned in an ultrasonic bath using detergent,

acetone and iso-propanol. After drying the slides, 70 μl of poly (3,4-ethylenedioxythiophene)/(poly(styrenesulfonate) (PEDOT:PSS, Baytron P) solution was spin-coated onto each ITO slide at 4000 rpm for 90 seconds with an acceleration of 1680 rpm per second to give an ~50 nm thick film. Immediately prior to deposition the PEDOT:PSS solution was filtered through a 0.45 μm PECD syringe filter to remove any large aggregates. The PEDOT:PSS coated substrates were then placed on a hotplate and dried at 140 °C for 30 minutes. For the active layers used in this study P3HT and PCBM were dissolved in a 1:0.8 by weight ratio in chloroform with a total concentration of 18 mg/ml. The solutions were sonicated for 60 minutes to aid dissolution. Once dissolved the solution was transferred to an inert atmosphere (N_2) glove-box, along with the PEDOT:PSS coated cells for active layer deposition. The P3HT:PCBM solution was deposited by pipetting 65 μl of solution onto each PEDOT:PSS covered substrate and then spreading it evenly across the surface using the pipette tip. The substrate was then spun at 2000 rpm for one minute (1680 rpm/s acceleration) to create a thin film of thickness 60 – 90 nm. Film-coated substrates were transferred to a hotplate in the glove-box and heated at 50 °C for 10 minutes to aid the removal of chloroform before evaporating the top layer aluminium cathode. All evaporative deposition of the aluminium took place at a pressure lower than 2 x 10^{-6} Torr using an Ångstrom Engineering evaporator. The series of aluminium-only electrodes deposited were designed to have individual layer thickness of 5 nm, 10 nm, 20 nm, 40 nm, 60 nm and 90 nm. Each film was deposited at a rate of 2 Å/s and control over thickness of the aluminium deposited was achieved by closing the evaporator shutter when the rate and time product met the desired thickness value. The area of each cell is 5 mm^2.

Device characterization

Current-voltage (I-V) measurements were conducted using a Newport Class A solar simulator with an AM 1.5 spectrum filter to illuminate the full cells. The light intensity was measured to be 100 mW/cm^2 by a silicon reference solar cell (FHG-ISE), and the I-V data were recorded by a Keithley 2400 source meter. All presented device characteristics are obtained from unmasked cells, annealed for 4 minutes at 140 °C under dry N_2. In order to determine directly the vertical composition of the P3HT:PCBM devices, X-ray photoelectron spectroscopy (XPS) depth profiling measurements using an Argon sputtering source were conducted on annealed and unannealed devices for aluminium-only cathodes with thickness of 5 nm, 40 nm, and 90 nm.

Equivalent circuit modelling

The equivalent circuit model fitting to the experimental data was performed using the MATLAB optimisation toolbox. Specifically, the *lsqcurvefit* function was used to determine the initial value of each parameter in the model while the *fzero* function was used to fit the experiment I-V characteristic using model-fit parameters.
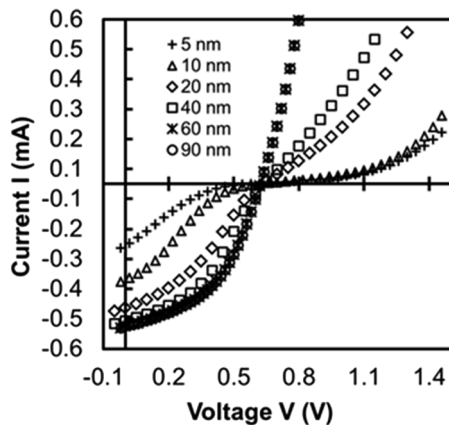
FIG. 1. I-V characteristics of P3HT:PCBM OPV devices for aluminium cathode thicknesses of: 5, 10, 20, 40, 60 and 90 nm. The thinner the aluminium cathode layer, the more pronounced the 'S' shape of the I-V curve.

RESULTS AND DISCUSSION

Figure 1 shows the I-V characteristics of the fabricated P3HT:PCBM OPV devices as a function of aluminium cathode thickness. The corresponding photovoltaic properties are summarized in Table I. As expected, it is clear that the I-V curves vary systematically from 'S' to 'J' shaped with increasing aluminium cathode thickness.

Figure 2 shows the variation of each device parameter as a function of aluminium cathode thickness as the I-V curve shape changes from 'S' to 'J' shaped. In general, the device short circuit current (I_{sc}), fill factor (FF), and efficiency (η) all increase systematically with increasing aluminium cathode thickness whereas the open circuit voltage (V_{oc}) is largely invariant for thicknesses above 10 nm. Previous studies that have shown that the V_{oc} in these devices is largely dependent upon the composition of the active layer blend materials[7,11,12] or the electrode material (work function);[13,21] suggesting that these quantities are not changing dramatically with increasing aluminium thickness above 10 nm.

The variation in the calculated cell efficiency values are directly mirrored in the changes in the fill factor (FF) values but interestingly, I_{sc} does not follow exactly the same behaviour. In addition, while both I_{sc} and FF increase with

increasing aluminium cathode thickness, R_s decreases and R_{sh} increases with increasing aluminium cathode thickness. The fact that both I_{sc} and FF improve with increasing aluminium cathode thickness indicates that it is the nature of the polymer-cathode interface that is changing and that these interfacial changes affect both R_{sh} and R_s. FF is sensitive to R_{sh} (driven by recombination processes) while both FF and I_{sc} are sensitive to R_s (driven by charge carrier generation and transport processes).[22] Consequently, it is this difference in sensitivities that results in I_{sc} rising more slowly than FF as aluminium cathode thickness increases. As such, these differences in the dependency of Isc and FF upon aluminium film thickness are a signature of changes in the nature or quality of the polymer cathode interface, the details of which are elaborated upon later in the paper. The observation that both I_{sc} and FF approach an asymptotic value when the top electrode reaches a critical thickness and conductivity approaches that of the bulk aluminium indicates that at this point the polymer cathode interface quality has improved substantially.

Figure 3 shows the model fits to the experimental I-V data for each aluminium cathode thickness and reveals that the equivalent circuit modelling provides an excellent match with the I-V characteristics. The extracted model-fit parameters are summarized in Table II where the B2BDM[17] is used to fit all 'S' shaped I-V curves (with a $V_{offset} \neq 0$ V) and the TDM (with R_{sh2} as a fitting parameter[11]) is used to fit all of the 'J' shaped I-V curves (the circuit models and basic equations are reproduced in supplementary material). The main reason for using the TDM is that this model is better able to accommodate the loss of current through pinholes (or other device shortage mechanisms due to porosity in OPV cells) by introducing a second shunt resistance, R_{sh2},[11] whilst also reducing the number of circuit elements and hence avoiding overfitting of the 'J' shaped I-V curves. The fits clearly show that these results perfectly support the earlier contact resistance explanation for 'S' shaped I-V curve generation as we can see that the series resistance R_s decreases with the increasing thickness of the top electrode. Moreover, the B2BDM model fits indicate that the shunt resistance R_{sh} remains effectively invariant with increasing aluminium thickness, which suggests that changes to recombination in the device are due to changes at the interface and not in the bulk active layer; consistent with our previous hypothesis.

By contrast, the photocurrent I_{ph} increases with increasing aluminium cathode thickness for all devices made from the

TABLE I. The average value and standard deviation of the OPV device characteristics as a function of aluminium cathode thickness.

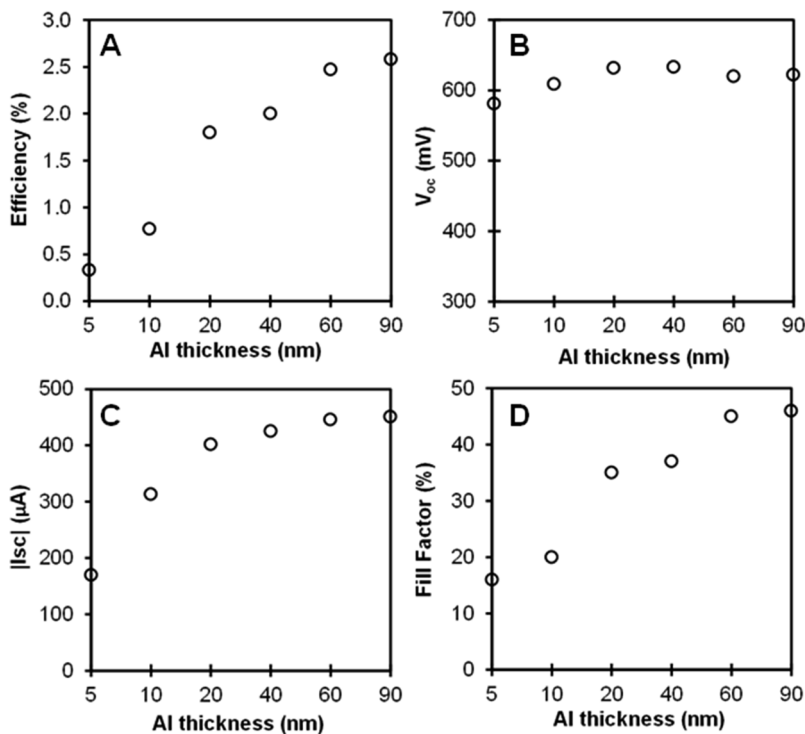| Sample	Cathode Thickness (nm)	Average OPV Characteristics			
		Voc (mV)	I_{sc} (μA)	FF (%)	Efficiency (%)
A	5	580.7 ± 10.9	170 ± 22	16 ± 0.4	0.33 ± 0.052
B	10	609.0 ± 6.0	313 ± 5	20 ± 1.1	0.77 ± 0.056
C	20	631.6 ± 1.6	402 ± 12	35 ± 1.3	1.80 ± 0.097
D	40	632.9 ± 1.5	425 ± 26	37 ± 2.6	2.00 ± 0.263
E	60	619.9 ± 8.3	446 ± 32	45 ± 0.7	2.47 ± 0.211
F	90	622.1 ± 1.9	451 ± 13	46 ± 0.7	2.58 ± 0.088

FIG. 2. OPV device characteristics as a function of aluminium cathode thickness. A: Power conversion efficiency, B: Open circuit voltage, C: Short circuit current, D: Fill factor. The average values of the devices characteristics of 12 cells (2 substrates) are plotted. The corresponding standard deviation values can be seen in Table I.

same active layer and illuminated under the same light conditions. Thus, photocurrent is controlled by the thickness of the top electrode similar to I_{sc}. Reduced recombination at the interface increases both the I_{sc} and the I_{ph} in the devices as the thickness of the aluminium cathode increases. A similar trend is also found with V_{offset} and n_3 both increasing with thicker aluminium electrodes using the B2BDM. In this case the V_{offset} and n_3 may be considered proxy measures for the "ideality" of the I-V curve shape.
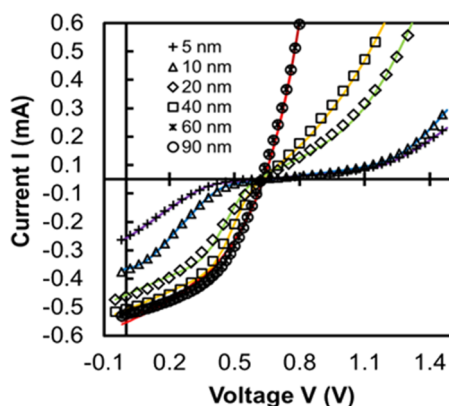

FIG. 3. The experimental (marked) and fitted I-V curves (coloured solid lines) where the B2BDM was used for the I-V data corresponding to aluminium cathode thicknesses of 5 nm, 10 nm, 20 nm, and 40 nm I-V data whereas the TDM was used for the I-V data corresponding to aluminium cathode thicknesses of 60 nm and 90 nm.

Figure 4 shows the XPS depth profiles for the unannealed and annealed OPV devices with representative aluminium cathode thicknesses of 5, 40 and 90 nm. The unannealed 5 nm aluminium cathode device (Figure 4(a)) clearly shows that the thin layer of deposited aluminium is largely oxidised to Al_2O_3 and associated hydroxide species, since a metallic Al 2p atomic percentage of only ~20% is seen. Similarly, a complete layer of Al_2O_3 is not reached either since the maximum Al(ox) 2p level obtained is ~30% and the corresponding O 1s level is ~45%, rather than the 40% and 60%, respectively, required for a complete, pure, oxide layer. Consequently the 5 nm "Al cathode" appears to be composed of a mixture of Al and Al_2O_3 in an approximate 20:80 ratio.

By contrast a pure (or almost pure, >90% Al) aluminium layer is observed for the two thicker cathodes with a reduced amount of oxide seen at the cathode active layer interface. There is very little change to the aluminium and aluminium oxide levels upon annealing of all of the devices indicating that oxidation of the aluminium occurs during the deposition process prior to the annealing stage. Interestingly, this oxidation occurs despite the fact that film deposition and annealing is conducted either under vacuum or in an oxygen-free N_2 atmosphere.

These composition plots provide a clear picture as to why a high series resistance is observed for the 5 nm cathode relative to the 40 nm and 90 nm cathode devices. Since the conductivity of aluminium oxide (~10^{-12} S/m)[23] is much lower than that of pure aluminium (3.583 x 10^7 S/m)[24] the highly oxidised electrode is inherently more highly resistive. However, the XPS profiles also indicate that complete

TABLE II. The model parameters extracted from the equivalent circuit modelling of the I-V profiles for different aluminium cathode thicknesses. All of the 'S' shaped I-V data (cathode thicknesses of 5, 10, 20 and 40 nm) are modelled by the B2BDM whereas the 'J' shaped I-V curves (cathode thicknesses of 60 and 90 nm) a modelled by the TDM. All of the model-fit parameters depend on the chosen model but note that $R_{sh} = R_{sh1}$ = shunt resistance in both the B2BDM and TDM.

Cathode Thickness (nm)	Model-fitted parameters								
	I_{o1} (µA)	I_{o2} (µA)	I_{o3} (µA)	I_{ph} (µA)	n_3	R_s (Ω)	R_{sh1} (kΩ)	R_{sh2} (kΩ)	V_{offset} (V)
5	176	44.5	1.9E−8	86.4	2.09	1400	700	15.0	0.368
10	137	140	3.2E−8	193	2.21	800	30.0	15.0	0.382
20	104	135	3.2E−3	182	3.80	324	3.00	35.0	0.502
40	148	97.4	7.06	206	9.81	202	2.00	35.0	0.537
	I_{o1} (µA)	I_{o2} (nA)	I_{ph} (µA)	n_1	n_2	R_s (Ω)	R_{sh1} (kΩ)	R_{sh2} (MΩ)	V_{offset} (V)
60	4.51	4.61	503	5.9	3.0	53.7	3.27	7.85	0
90	6.16	2.69	513	6.2	2.9	54.8	3.38	3.97	0

layers of aluminium oxide do not exist either on the top of the aluminium cathodes or at the cathode active layer interfaces. Consequently, the aluminium oxide layers are discontinuous and porous and as such are probably in the form of aluminium oxide clusters.

According to Glatthaar et al., 'S' shaped I-V curves can arise following a very fast deposition of the top aluminium electrode; resulting in a poorly conducting depletion region at the metal contact.[25] In this case, however, all of the different aluminium cathodes thicknesses were evaporated at the same deposition rate. They also stated that this kink is not caused by a counter diode but by a slow charge transfer at one of the electrical contacts of the absorber layer. However, the excellent fits of the 'S' shaped data to the B2BDM demonstrates that an effective counter diode is present in these cases, while the XPS depth profiling results confirm that the diode arises from the presence of interfacial oxidised aluminium.

The presence of aluminium oxide at the active layer/ cathode interface can be explained by two potential mechanisms. One possibility is that oxidising material (e.g. oxygen or water) can diffuse through the active layer or via pinholes in the evaporated aluminium layer resulting in oxidation at the interface.[26] Alternatively, adventitious adsorbed oxygen/water at the active layer surface could oxidise the aluminium as it is deposited. Previous studies have shown that aluminium metallisation of polymers is characterised by intermixing at the polymer-metal interface followed by aluminium cluster formation.[27] For aluminium evaporated on P3HT, it has also been shown that initial aluminium oxide formation at the polymer-electrode interface is followed by the formation of metallic aluminium as the thickness of aluminium is increased.[28] Combining these XPS depth profiles with the previous studies provides a more complete picture of the structural changes that occur within the aluminium cathode as its thickness increases. At very low aluminium coverages (5 nm), the cathode consists of an almost entirely oxidised porous layer characterised by an 'S' shaped I-V profile arising from extensive charge trapping in the interlayer region. The discontinuous and porous nature of the very thin aluminium film allows oxygen and water to penetrate through the

film to oxidise the interface. As the aluminium cathode thickness increases, the pinholes in the aluminium later start to fill and the layer becomes increasingly metallic; reducing the 'S' shaped character of the I-V plot. Aluminium oxide forms at the cathode surface, but now starts to passivate the top of the electrode and the transport of oxidising species to the interface is reduced (Figure 5). Finally, for the thick (>60 nm) cathode layers the concentration of aluminium oxide at the interface is now much lower than the pure aluminium concentration resulting in an ohmic contact and a 'J' shaped I-V profile.

Whilst annealing the devices does not alter the degree of oxidation of the cathode, it does result in major changes in the morphology of the active layer.[29-32] In particular, the carbon:sulphur (C:S) ratio for the active layer provides significant insights into the vertical composition of the devices. P3HT has a monomeric empirical formula of $C_{10}H_{14}S$ and a corresponding monomeric molecular weight of 166.28 g/mol. PCBM has a molecular formula of $C_{72}H_{14}O_2$ and a molecular weight of 910.88 g/mol. Consequently a pure active layer with a blend ratio of P3HT:PCBM 1:0.8 should display a C:S ratio of 20.52:1. This calculation is in excellent agreement with the C:S ratios observed for all of the unannealed device architectures measured in this chapter (which all appear at 20.5 ± 10%). Similarly the PEDOT:PSS used in this study has a ratio of 1:2.5. PEDOT has a monomeric empirical formula of $C_6H_4O_2$. PSS has a monomeric empirical formula of approximately $C_8H_9SO_3$ (with some variation due to deprotonation of the sulphonic acid, replacement of the proton by a sodium ion and associated water of hydration). Thus a ratio of approximately 10.4:1 should be observed for a pure PEDOT:PSS layer. Again this value agrees excellently with the PEDOT:PSS plateau region in the C:S ratio plot at longer etch time, and adjacent to, the active layer.

Upon annealing dramatic increases are observed in the C:S ratio at the cathode/active layer interface for the devices with 5 nm and 40 nm thick aluminium cathodes, with these values increasing to >35 and >45, respectively. These changes in C:S ratio correspond to an approximate 2.4 fold and 3.3 fold increase, respectively, in the amount of PCBM in the active
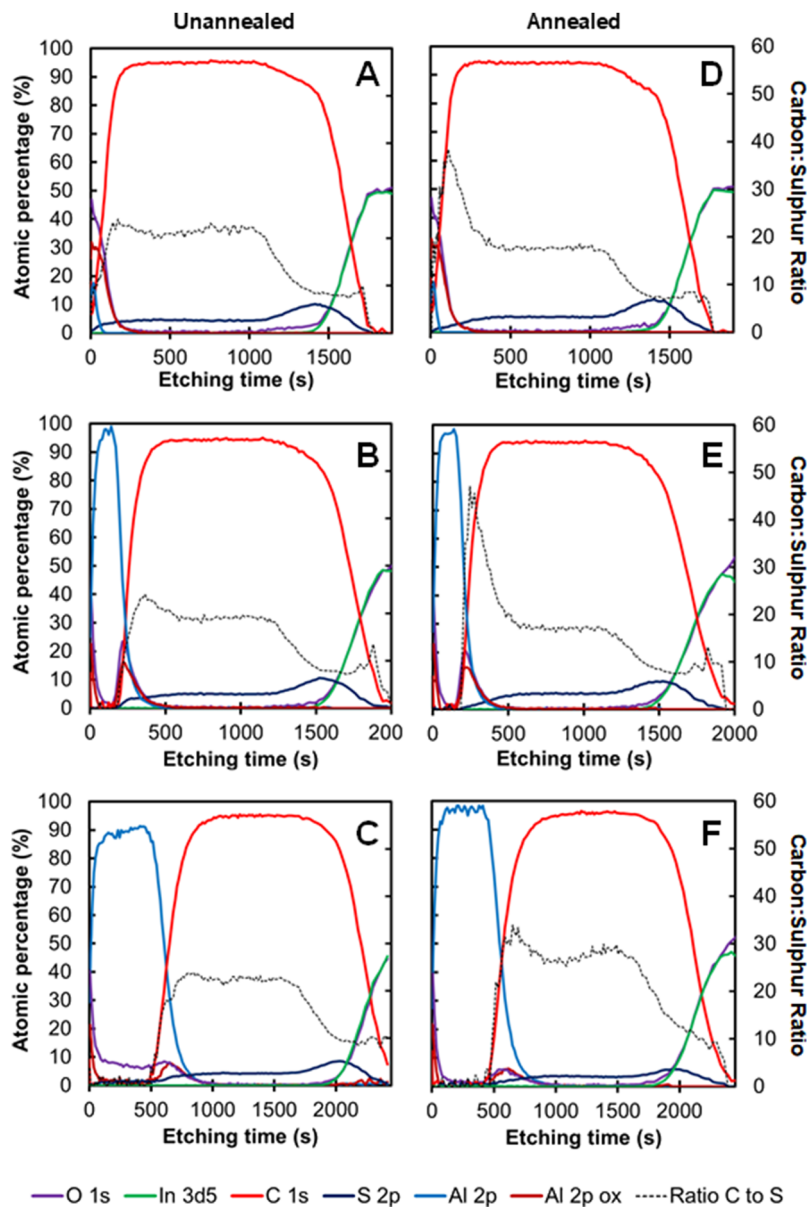
FIG. 4. XPS concentration depth profiles for OPV devices with a top electrode of aluminium of different thicknesses. Panels A, B and C show the depth profiles for unannealed OPV devices with a top aluminium cathode thickness of 5 nm, 40 nm and 90 nm respectively. Panels D, E and F show the depth profiles for annealed OPV devices with a top aluminium cathode thickness of 5 nm, 40 nm and 90 nm respectively.

layer at the cathode interface of these two devices and is consistent with vertical phase segregation in the active layer driven by the presence of an aluminium oxide interface. This segregation improves OPV function since it concentrates the electron transport material at the cathode interface. By contrast the change in the C:S ratio for the 90 nm aluminium cathode is much more modest and correlates with reduced aluminium oxide at the cathode interface. This observation supports the premise that pinholes provide a key pathway for aluminium oxidation at the active layer/cathode interface and that by increasing the aluminium layer thickness pinhole density decreases and oxidation is mitigated. The reduced concentration of aluminium oxide clearly decreases the drive

for PCBM to migrate to the active layer/cathode interface even upon annealing. Previous work has shown that P3HT acts to block aluminium penetration whereas PCBM facilitates movement of aluminium into the active layer.[33] Here we show that aluminium oxide at the interface also acts to prevent aluminium penetration into the active layer as evidenced by the relative increase in the Al 2p concentration within the C 1s region (Figure 4E and Figure 4F).

How do the optimised parameters of the B2BDM relate to the findings of the XPS analysis, especially the equivalent circuit components that determine the corrected photocurrent? As well as affecting the series resistance, R_s, of the OPV, the existence of a mix of pure aluminium and aluminium oxide,
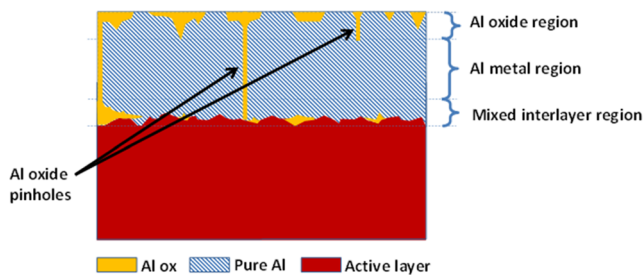
FIG. 5. Structural model derived from XPS depth profiling of P3HT:PCBM OPV devices with evaporated aluminium cathode of intermediate thickness. The vertical structure comprises: a mixed aluminium metal and aluminium oxide interface layer, an aluminium metal-rich bulk cathode region and an oxidised aluminium passivating surface.

especially at the cathode/active layer interface results in two parallel interfaces which relate to the back to back diode in the B2BDM. At a certain external voltage, charges will move into the aluminium oxide since it has a lower work function than the pure aluminium. This process slows charge extraction; resulting in charge trapping in islands of aluminium oxide and correlates to D_1 in the B2BDM. Under these conditions the intrinsic internal field of the OPV is lowered and charges accumulate at the interface; resulting in the observed space charging effect and charge recombination. This physical process is represented in the equivalent circuit model by the offset voltage, V_{offset}, while the charge recombination is represented by the shunt resistance, R_{sh1}. With increasing aluminium cathode thickness, V_{offset} increases systematically; shifting towards V_{oc} while R_{sh1} decreases systematically (from 700 kΩ to 2 kΩ); reducing the relative contribution of the back-to-back diodes. Increasing the external voltage, V, rectifies the diode characteristic of the interface, represented by D_3. The rate of charge extraction is increased and trapped charges are released. By contrast, under reverse bias, rectification occurs at the non-ohmic contact produced at the

anode interface, corresponding to D_2 in the B2BDM, and acts to decrease current flow.

Further evidence for charge trapping in OPV devices with thin aluminium cathodes is highlighted in Figure 6, which shows the dynamic resistance (R_d) of the OPV devices as a function of aluminium thickness. Interestingly, these plots show that cell resistivity is highly voltage dependant. Cells with thicker (60 nm and 90 nm) evaporated aluminium cathodes, which have a normal 'J' shaped I-V curve, exhibit a systematic decreasing of resistance with increasing voltage. By contrast, all cells with a thinner evaporated aluminium thickness, and a pronounced 'S' shaped I-V curve, exhibit a maximum in R_d that occurs beyond the V_{oc} of the cell; e.g a cell with a 5 nm thick aluminium cathode has V_{oc} = 0.581 V but the R_d peak occurs at 0.66 V.

These plots show that for an ideal 'J' shaped I-V characteristic charge extraction becomes more facile as the device voltage approaches V_{oc}. However, for an 'S' shaped I-V profile the resistance of the cell rises dramatically as V_{oc} is approached since charge trapping and the corresponding space-charge build-up results in a reduction in the expected charge extraction.

CONCLUSION

The effect of varying aluminium cathode thickness upon OPV device performance in both the 'S' and 'J' shaped I-V curve regimes have been probed by a combination of equivalent circuit modelling and XPS depth profiling. As expected, the results highlight that the 'S' shaped IV curve arises from charge trapping due to the presence of highly oxidised aluminium at the active-layer/cathode interface. This situation is modelled extremely well by the B2BDM, with the circuit elements in the model correlating with the physical features observed in the depth profile. For example, the behaviour of the diode (D_1) at the active layer cathode interface and the offset voltage (V_{offset}) change systematically as the cathode layer increases and the interfacial aluminium oxide concentration reduces. This work validates the B2BDM as a tool for analysing IV profiles.

SUPPLEMENTARY MATERIAL

See supplementary material for B2BDM and TDM circuit models and basic equations.
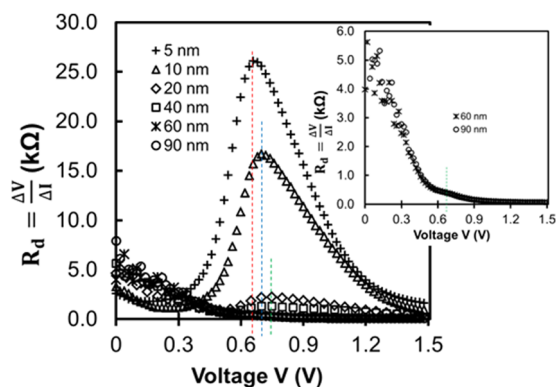
ACKNOWLEDGMENTS

FIG. 6. The dynamic resistance (R_d) as a function of applied voltage as a function of aluminium cathode thickness for aluminium cathode thicknesses of 5, 10, 20, 40, 60 and 90 nm. Inset: The R_d as a function of applied voltage only for devices with aluminium cathode thicknesses of 60 and 90 nm.

REFERENCES

[1] G. Pirotte, J. Kesters, P. Verstappen, S. Govaerts, J. Manca, L. Lutsen, D. Vanderzande, and W. Maes, ChemSusChem **8**, 3228 (2015).

[2] M. Glatthaar, M. Riede, N. Keegan, K. Sylvester-Hvid, B. Zimmermann, M. Niggemann, A. Hinsch, and A. Gombert, Sol. Energy Mater. Sol. Cells **91**, 390 (2007).

[3] F. J. García-Sánchez, B. Romero, D. C. Lugo-Muñoz, G. Del Pozo, B. Arredondo, J. J. Liou, and A. Ortiz-Conde, FU Elect. Energ. **30**, 327 (2017).

[4] F. A. de Castro, J. Heier, F. Nuesch, and R. Hany, IEEE J. Sel. Top. Quantum Electron. **16**, 1690 (2010).

[5] A. Wagenpfahl, D. Rauh, M. Binder, C. Deibel, and V. Dyakonov, Phys. Rev. B **82**, 115306 (2010).

[6] A. Kumar, S. Sista, and Y. Yang, J. Appl. Phys. **105**, 094512 (2009).

[7] J. C. Wang, X. C. Ren, S. Q. Shi, C. W. Leung, and P. K. L. Chan, Org. Elec. **12**, 880 (2011).

[8] L. Zuo, J. Yao, H. Li, and H. Chen, Sol. Energy Mater. Sol. Cells **122**, 88 (2014).

[9] K. Tada, Org. Elec. **40**, 8 (2017).

[10] B. Y. Finck and B. J. Schwartz, Appl. Phys. Lett. **103**, 053306 (2013).

[11] A. Moliton and J.-M. Nunzi, Polym. Int. **55**, 583 (2006).

[12] A. Cheknane, H. S. Hilal, F. Djeffal, B. Benyoucef, and J.-P. Charles, Microelectron. J. **39**, 1173 (2008).

[13] W. J. Potscavage, A. Sharma, and B. Kippelen, Acc. Chem. Res. **42**, 1758 (2009).

[14] E. Sesa, "A novel electrical model for organic photovoltaic cells," Ph.D. thesis, University of Newcastle, Australia, 2013.

[15] M. M. Furchi, A. A. Zechmeister, F. Hoeller, S. Wachter, A. Pospischil, and T. Mueller, IEEE J. Sel. Top. Quant. Electron. **23**, 106–116 (2017).

[16] A. Pozza, G. Bardizza, T. Sample, and E. Dunlop, Proc. 29th Europ. Photovol. Sol. Energy Conf (2014) 1523–1529.

[17] E. Sesa, B. Vaughan, K. Feron, C. Bilen, X. Zhou, W. Belcher, and P. Dastoor, Org. Elec. **58**, 207 (2018).

[18] D. S. Pillai, B. Sahoo, J. P. Ram, A. Laudani, N. Rajasekar, and N. Sudhakar, Energy Procedia **117**, 1054 (2017).

[19] A. Laudani, F. Riganti Fulginei, F. De Castro, and A. Salvini, Sol. Energy **163**, 526 (2018).

[20] C. Xu, F. Yu, W. Lin, and G. Huang, Crystals **8**, 277 (2018).

[21] V. K. Agarwala and T. Fort, Jr., Surf. Sci. **54**, 60 (1976).

[22] D. Gupta, M. Bag, and K. S. Narayana, Appl. Phys. Lett. **92**, 093301 (2008).

[23] MIT, Material Property Database - Aluminium oxide [cited 2013 12 January]; Available from: http://www.mit.edu/~6.777/matprops/alox.htm.

[24] MIT, Material Property Database - Aluminium [cited 2012 12 January]; Available from: http://www.mit.edu/~6.777/matprops/aluminum.htm.

[25] M. Glatthaar, M. Riede, N. Keegan, K. Sylvester-Hvid, B. Zimmermann, M. Niggemann, A. Hinsch, and A. Gombert, Sol. Energy Mater. Sol. Cells **91**, 390 (2007).

[26] K. Feron, T. J. Nagle, L. J. Rozanski, B. B. Gong, and C. J. Fell, Sol. Energy Mater. Sol. Cells **109**, 169 (2013).

[27] P. S. Ho, P. O. Hahn, J. W. Barth, G. W. Rubloff, F. K. LeGoues, and B. D. Silverman, J. Vac. Sci. Technol. A **3**, 739 (1985).

[28] H. Y. Seung and J. E. Whitten, Synth. Met. **114**, 305 (2000).

[29] M. Campoy-Quiles, T. Ferenczi, T. Agostinelli, P. G. Etchegoin, Y. Kim, T. D. Anthopoulos, P. N. Stavrinou, D. D. Bradley, and J. Nelson, Nature Mater. **7**, 158 (2008).

[30] Z. Xu, L.-M. Chen, G. Yang, C.-H. Huang, J. Hou, Y. Wu, G. Li, C.-S. Hsu, and Y. Yang, Adv. Funct. Mater. **19**, 1227 (2009).

[31] L. M. Chen, H. Ziruo, G. Li, and Y. Yang, Adv. Mater. **21**, 1434 (2009).

[32] A. Orimo, K. Masuda, S. Honda, H. Benten, S. Ito, H. Ohkita, and H. Tsuji, Appl. Phys. Lett. **96**, 043305 (2010).

[33] G. Zhang, S. A. Hawks, C. Ngo, L. T. Schelhas, D. T. Scholes, H. Kang, J. C. Aguirre, S. H. Tolbert, and B. J. Schwartz, ACS Appl. Mater. Inter. **7**, 25247–25258 (2015).

Circuit Element and Device Function Relationships in Circuit Models:

Validating the Back-to-Back Diode Model for Organic Photovoltaics

Elisa Sesa[1], Darmawati Darwis[1], Dedy Farhamsah[1], Xiaojing Zhou[2], Warwick J. Belcher[2], Paul C. Dastoor[2]
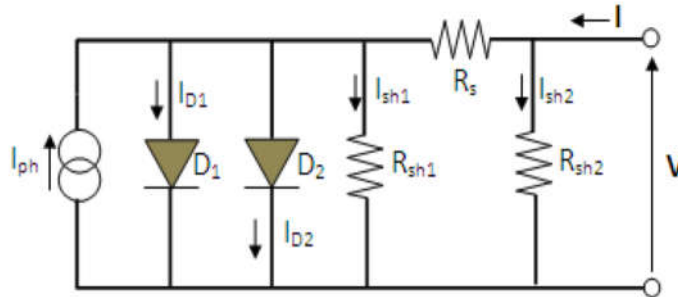
[1]Physics Department, University of Tadulako, Palu, Indonesia

[2]Centre for Organic Electronics, University of Newcastle, Callaghan, NSW 2308, Australia

Supplementary Information

Two Diode Model (TDM)

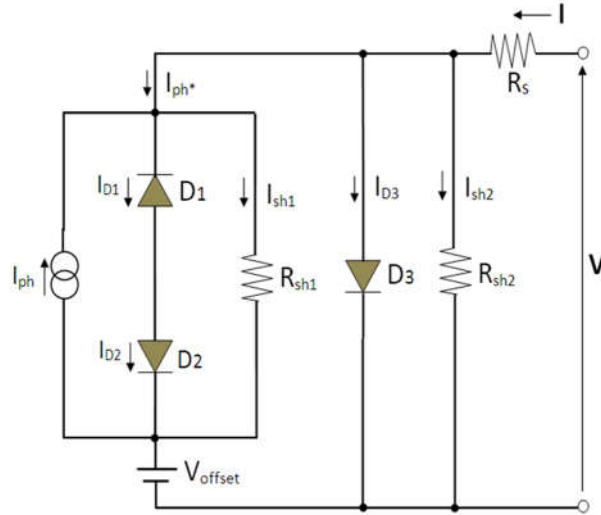The TDM circuit diagram and governing equation [**Ошибка! Источник ссылки не найден.**].

$$I = -I_{ph} + I_{01}\left[\exp\left(\frac{q\left(V\left(1+\frac{R_s}{R_{sh2}}\right)-IR_s\right)}{n_1 kT}\right)-1\right] + I_{02}\left[\exp\left(\frac{q\left(V\left(1+\frac{R_s}{R_{sh2}}\right)-IR_s\right)}{n_2 kT}\right)-1\right] + \frac{V\left(1+\frac{R_s}{R_{sh2}}\right)-IR_s}{R_{sh1}} + \frac{V}{R_{sh2}}$$

Back to Back Diode Model (B2BDM)

The B2BDM circuit diagram and governing equation [**Ошибка! Источник ссылки не найден.**].

$$I = -I_{ph} + \frac{V - IR_s - V_{offset}}{R_{sh1}} + \frac{I_{01}I_{02}\left[\exp\left(\frac{q\left(V - IR_s - V_{offset}\right)}{kT}\right) - 1\right]}{I_{01}\exp\left(\frac{q\left(V - IR_s - V_{offset}\right)}{kT}\right) + I_{02}} + I_{03}\left[\exp\left(\frac{q\left(V - IR_s\right)}{n_3 kT}\right) - 1\right] + \frac{V - IR_s}{R_{sh2}}$$